Algorithm, Progresses, Datasets and Validation of GLC_FCS30D: the first global 30 m land-cover dynamic product with fine classification system from 1985 to 2022

Liangyun Liu[1,2,3] and Xiao Zhang[1,2]

[1] International Research Center of Big Data for Sustainable Development Goals, Beijing 100094, China
[2] Key Laboratory of Digital Earth Science, Aerospace Information Research Institute, Chinese Academy of Sciences, Beijing 100094, China
[3] School of Electronic, Electrical and Communication Engineering, University of Chinese Academy of Sciences, Beijing 100049, China

KEY WORDS: global land-cover, Landsat imagery, time-series, continuous change detection, GLC_FCS30D.

ABSTRACT:
Land cover change information plays an indispensable role in environmental monitoring, climate change research, agricultural planning, urban development, biodiversity conservation, and natural disaster risk assessment. Recently, the free access of Landsat imagery and improvement of computation capacity especially supported by Google Earth Engine platform provides great chance in time-series land-cover change monitoring. We used the stratified land-cover monitoring strategy and time-series Landsat imagery to develop a novel global 30 m land-cover dynamic product with fine classification system from 1985 to 2022 (GLC_FCS30D). Firstly, we used the multitemporal classification to generate the time-series impervious surfaces, wetlands and tidal flat products. Then, we proposed to combine the continuous change detection algorithm and local adaptive updating model to capture the land-cover changes, and to generate a new global 30 m land-cover dynamic product (impervious surfaces, wetlands and tidal flat types were excluded in this step). Next, after overlapping the three multitemporal classification products and the time-series dynamical land-cover dataset, the novel GLC_FCS30D was developed, which contained 35 fine land-cover types. Lastly, using the global 84526 validation points in 2020, the GLC_FCS30D was validated to show the great performance with an overall accuracy of 80.88%, and had obvious advantages over other global land-cover products in diversity of land-cover types and mapping accuracy.

1. INTRODUCTION

Land cover and its change information is vital and basic information in climate-change analysis, ecological environment assessment, food security research and sustainable development (Liu et al., 2021; Zhang et al., 2021b; Zhang et al., 2019; Zhang et al., 2018). Over the last millennium, approximately 3/4 earth’s land surfaces experienced the land-cover changes (Winkler et al., 2021). As the global population grows and economic development demands, this rate of land cover change is accelerating (Zhang et al., 2024b), which directly caused a series of ecological and environment issues such as: global warming, extreme climate, rising sea levels, etc. (Song et al., 2018). Thus, understanding and quantifying the global land-cover changes and its temporal dynamic is greatly important in pursuing the sustainable development goals.

Remote sensing technique, owning to its large-scale and repeated observations, has been widely used to land-cover mapping and change monitoring (Chen et al., 2015; Friedl et al., 2010; Wang et al., 2023; Zhang et al., 2024b). Overall, the land-cover mapping have made great progresses and continually released a lot of global land-cover products, ranging from 1km to 10 m, which provides important support for understanding the current status of land cover (Ban et al., 2015; Grekousis et al., 2015). Comparatively, how to accurately capture the land-cover changes from the multitemporal satellite observations was more difficult, and the corresponding global land-cover dynamic products are also sparser. Nowadays, there are two widely used and coarse land-cover dynamic datasets (MCD12Q1 (Friedl et al., 2010) and CCI_LC (Defourny et al., 2016)), both of them gave global land-cover change information every year and spanned the period more than 20 years. However, the previous work in Song et al. (2018) demonstrated that the 60% global land-cover changes associated with human activities, and human-induced changes were usually fragmented and small. Namely, the coarse global land-cover dynamic products cannot fulfil the goal of accurately quantifying the global land-cover changes.

Recently, the improvement of computation capacity and free-access the medium-resolution satellite imagery (especially for the open access of Landsat in 2008 (Woodcock et al., 2008)) gave great opportunity in the high-resolution land-cover change monitoring. For example, the multitemporal GlobeLand30 products in 2000, 2010 and 2020 were developed by combining time-series Landsat imagery and POK (pixel- and object-based methods with knowledge) based method (Chen et al., 2015). These sparse temporal global land-cover dynamic products can capture land-cover change details but miss the land-cover change process and some short-time changes (cropland fallow). So, the annual land-cover change monitoring has been pursuing and also generate some products (Friedl et al., 2022; Potapov et al., 2022; Xian et al., 2022; Yang and Huang, 2021). For example, Friedl et al. (2022) used all available Landsat observations to generate annual 30 m maps of global land-cover during 2001-2020 (named as: GLanCE) and achieved good accuracy of 77.0±2.0%. This dataset is an important milestone because it was the first global 30 m annual land-cover maps, however, its simple classification system (containing seven land-cover types) and lacking of land-cover change information before 2000 might affect its widespread use.

In this study, we present a novel global 30 m land-cover dynamic product with fine classification system (named as: GLC_FCS30D), which contains 35 fine land-cover types, covers the long periods from 1985 to 2022 with 26 time-steps (1985, 1990, 1995, 2000, 2001, 2002, …, 2021, 2022). The 5-years updating cycle before 2000 is because the sparse availability of Landsat imagery (Roy et al., 2014). The goal of the study is to describe the basic principle of the methods, the performance of data products and the land-cover change analysis of GLC_FCS30D, while the specific details can be followed at corresponding data description articles.

2. METHODS

We used the stratified land-cover monitoring strategy and time-series Landsat imagery to develop a novel global 30 m land-cover

This contribution has been peer-reviewed. The double-blind peer-review was conducted on the basis of the full paper.
https://doi.org/10.5194/isprs-annals-X-2-2024-137-2024 | © Author(s) 2024. CC BY 4.0 License.

dynamic product with fine classification system from 1985 to 2022 (GLC_FCS30D). Figure 1 illustrates the main flow of how to generate the GLC_FCS30D land-cover change monitoring datasets. It can be found that three multi-temporal thematic products (including, impervious surfaces, wetlands and tidal flats) are indepdentently developed (the land covers were independtly classified for each epoch). Then, we used the continuous change-detection algorithm and full time-series Landsat observations to generate the long time-series land-cover dynamic dataset for othe land cover types. Finally, we combined the three multi-temporal thematic products and the long time-series land-cover dynamic dataset to create the comprehensive GLC_FCS30D.

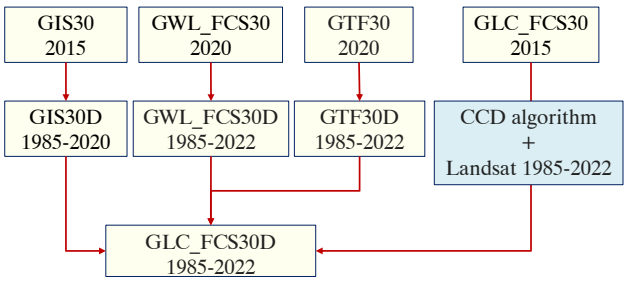

Figure 1. The main flow of how to generate the GLC_FCS30D dataset.

2.1 GISD30: the global 30 m impervious surface dynamic products

The impervious surface is independently developed because it is a human-induced land-cover type and spatial fragmented and spectral heterogeneity (Zhang et al., 2021a; Zhang et al., 2020). Although a lot of works have been paid to capture impervious surface expansion, most works concentrated on the urban areas, that is, the small and fragmented rural areas usually suffered the obvious omission and commission errors (Wang et al., 2022). To accurately capture global impervious surface dynamics and solve the problem of collecting training samples, we proposed a novel automated monitoring strategy for capturing impervious surface dynamics.

Specifically, we assumed that the land-cover conversion from natural surfaces to impervious surface is irreversible, and then derived the pervious surfaces and impervious surfaces training samples in 2020 from several existing impervious surface products (GAIA (Gong et al., 2020), GHSL (Florczyk et al., 2019), GlobeLand30 (Chen et al., 2015) and GLC_FCS30 (Zhang et al., 2021b)) after applying the refinement rules. Afterwards, we directly migrated the pervious surfaces training samples according to the irreversible assumption and simultaneously spectrally generalized impervious surface reflectance spectra in 2020 to other periods after radiometric normalization. Next, combining the generalized reflectance spectra of impervious surfaces and migrated pervious surface samples, the local adaptive random forest classification models were trained and the spatiotemporal consistency optimization algorithm was applied to develop the time-series impervious surface products (Zhang et al., 2022a).

In terms of the quality of GISD30, it was validated in the previous work in Zhang et al. (2022a) using 23322 globally distributed ground-truths samples with an overall accuracy of 90.1% and a kappa coefficient of 0.865, which were higher than other global 30 m impervious surface products. Meanwhile, the qualitative comparisons with other datasets also explained the superiority of the GISD30 in capturing the spatiotemporal dynamic of impervious surfaces in complex landscapes such as: rural areas, cloud-contamination tropical areas.

2.2 GWL_FCS30D: the global 30 m wetland dynamic products

Due to the serious spectral heterogeneity and quick temporal variations, there was great uncertainty in wetland mapping and dynamic monitoring (Pekel et al., 2016; Zhang et al., 2023b). More attentions were paid on the single wetland analysis (water body, mangrove forest, tidal flats) (Hu et al., 2017), and still lacking the comprehensive global 30 m wetland maps. Several open-access coarse wetland products still have significant differences in global wetland area (Guo et al., 2017), that is, the estimation of global wetlands is still challenging and necessary. To quantify the spatial distribution of global 30 m wetlands, we also develop a novel global 30 m wetland dynamic products (named as: GWL_FCS30D).

Table 1. The description of fine wetland classification system came from work of Zhang et al. (2023b).

Category I	Category II	Description
Tidal wetland	Mangrove	The forest or shrubs which grow in the coastal blackish or saline water
	Salt marsh	Herbaceous vegetation (grasses, herbs and low shrubs) in the upper coastal intertidal zone
	Tidal flat	The flooded zones between the coastal high and low tide levels including mudflats and sandflats.
Inland wetland	Swamp	The forest or shrubs which grow in the inland freshwater
	Marsh	Herbaceous vegetation (grasses, herbs and low shrubs) grows in the freshwater
	Flooded flat	The non-vegetated flooded areas along the rivers and lakes
	Saline	Characterized by saline soils and halophytic (salt tolerant) plant species along saline lakes
	Permanent water	Lakes, rivers and streams that are always flooded

Table 1 gave the description of the fine wetland classification system in the GWL_FCS30D, which contained two level-1 groups (inland wetland and coastal wetland), and further divided into 5 inland subcategories (swamp, marsh, flooded flat, saline and permanent water) and 3 coastal subcategories (mangrove, salt marsh and tidal flat) (Zhang et al., 2023b).

One of the biggest challenge in wetland mapping is how to collect the globally distributed training samples. To solve the problem, we proposed to make full use of these open-access global wetland products, and combine the visual interpretation, expert prior knowledge and some refinement rules to generate high-confidence training samples. Then, we generate the highest and lowest water-levels and phenological features from time-series Landsat and Sentinel-1 observations, and further adopted the stratified classification strategy and local adaptive classifications to develop the coastal wetland and inland wetland maps.

Using the globally distributed and confident training samples, multisourced and time-series satellite imagery, and stratified classification strategy, we characterize the 1985-2022 wetland dynamics at 30 m resolution (Zhang et al., 2024a). To ensure the spatiotemporal consistency of the GWL_FCS30D, the temporal consistency optimization algorithm, benefiting from the spatiotemporal pixels, to remove the ‘salt and pepper’ noise caused by the pixel-based classification in each wetland map.

In terms of the accuracy metrics of the GWL_FCS30D wetland maps, we firstly collected a total of 25708 validation points (including 15151 wetland points and 10558 non-wetland points) by integrating high-resolution imagery, time-series Landsat observations (auxiliary dataset) and visual interpretation. Then, the GWL_FCS30D was validated, giving an overall accuracy of

86.95±0.44% and a kappa coefficient of 0.822. Meanwhile, using the third-party time-series validation datasets (LCMAP(Stehman et al., 2012) and LUCAS (d'Andrimont et al., 2020)), our GWL_FCS30D also showed great stability in the producer's and user's accuracies (P.A. and U.A.), with an U.A. of 88.98%–90.52% in LCMAP dataset and 84.67%–85.71% in LUCAS dataset. (Zhang et al., 2024a).

2.3 GTF30D: the global 30 m tidal flat products

Tidal flat, as a special coastal wetland subcategory, was defined as the tidal flooding zones during the high and low tides of a coastal spring tide (Dyer et al., 2000). The tidal flats affected the daily tide variations, thus, how to accurately capture tidal flats' distribution and dynamic is also difficult. Although Murray et al. (2019) and Murray et al. (2022) proposed the classification-based method to generate the global 30 m tidal flat products, however, they cannot cover the high latitude areas in the Northern Hemisphere (>60° N) and were analyzed to suffer commission error (Jia et al., 2021; Zhang et al., 2022b). To characterize the global tidal flats (also covering the >60° N areas), we proposed an automated tidal flat mapping method by combining the lowest and highest tide information (Zhang et al., 2023a).

Specifically, we analyzed the spectra sensitivity of water body, tidal flats and inlands, and proposed a novel low tide index (name as: LTideI), which was demonstrated to be more robust and accurate in capturing the low tides from time-series satellite imagery. Then, we composited the lowest and highest tide information using the proposed LTideI index and time-series Landsat imagery to generate the potential tidal flat areas after using the Ostu algorithm (Otsu, 1979), and further import the prior tidal flat products and refinement rules to generate a globally distributed tidal flat training sample pool. Afterwards, the local adaptive random forest classifier at each 5° × 5° geographical tile (global coast was split into 588 tiles) was independently trained using the regional training samples and multi-temporal tide-level features. Finally, the time-series global 30 m tidal flat maps were generated, and the temporal changes of tidal flats were also captured (Zhang et al., 2023a).

In order to analyse the performance of GTF30D, a globally distributed validation dataset including 6,828 tidal flat points and 7,166 non-tidal flat points were collected. The overall accuracy and kappa coefficient metrics were calculated from the confusion matrix, and reached 90.34% and 0.807, respectively. Meanwhile, the cross-comparisons with other national and global tidal flat products also indicated that the GTF30D can be more accurate in capturing the tidal flats and supressing the commission error (Zhang et al., 2023a).

2.4 Monitoring global land-cover changes from continuous Landsat observations

In terms of the remaining land-cover changes, we proposed to use the continuous change detection (CCD, (Zhu and Woodcock, 2014; Zhu et al., 2012) to capture the time-points of land-cover changes. The key-point of CCD is to fit the time-series observations into two components: trend term, seasonal term as following equation:

$$\hat{\rho}(i,t) = a_{0,i} + c_{1,i} \times t + \sum_{k=1}^{n}\left(a_{k,i} \times cos\left(\frac{2k\pi}{T}t\right) + b_{k,i} \times sin\left(\frac{2k\pi}{T}t\right)\right)$$

Where the harmonic terms represented the seasonal variations, and the order of n was determined by the number of valid Landsat observations, and usually selected as 3 (Xian et al., 2022).

Using the CCD continuous land-cover change detection method, we can identify the temporal stable areas and the time-points of changed areas. As previous studies have demonstrated that the spatiotemporal stable areas usually achieved the higher accuracies (Radoux et al., 2014; Zhang and Roy, 2017), we further generate the spatiotemporal stable training samples from the temporal stable areas. Afterwards, we combined the phenological and texture features to train the random forest models at each 5°×5°(global land surfaces was split into 961 tiles) and then combine the changed information (deriving from CCD algorithm) to update their land-cover information (Zhang et al., 2024b).

To improve rationality of time-series land-cover changes, the spatiotemporal optimization algorithm was still necessary to supress the 'salt-and pepper' noisy caused by the pixel-based classifications. In the GLC_FCS30D products, the spatiotemporal homogeneity was calculated for each changed pixel in the local window of 3×3×3 (Zhang et al., 2024b). It should be noted that the GLC_FCS30D, only applying the change detection and dynamic updating, didn't contain impervious surface, wetland and tidal flat, thus, we needed to further overlay the GISD30, GWL_FCS30D and GTF30D into the GLC_FCS30D according to their definitions.

2.5 The validation of GLC_FCS30D dynamic products

Quantifying the performance of GLC_FCS30D was also an indispensable step, we collected a globally distributed validation datasets (name as: SRS_Val) (Zhao et al., 2023). It used the stratified random sampling strategy to increase the sample size in the heterogeneity areas and rare land-cover types, and collected by combining the visual interpretation, quality-controlling and multisourced auxiliary datasets based on the Google Earth Engine platform (https://eliza-ting.users.earthengine.app/view/crd-vit). It contained 84526 validation points at 17 fine land-cover types for the basic year of 2020.

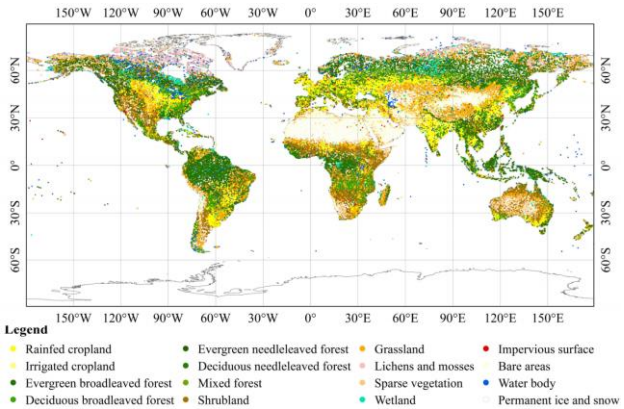

Figure 2. The spatial distribution of SRS_Val validation dataset in 2020, which came from our previous work in Zhao et al. (2023).

In terms of the accuracy metrics, four classical metrics, came from the confusion matrix, were calculated including: overall accuracy and kappa coefficient (measuring the comprehensive performance between the map and reference data), user's accuracy (measuring the omission error of each land-cover type) and producer's accuracy (measuring the commission error of each land-cover type) (Olofsson et al., 2014).

This contribution has been peer-reviewed. The double-blind peer-review was conducted on the basis of the full paper.
https://doi.org/10.5194/isprs-annals-X-2-2024-137-2024 | © Author(s) 2024. CC BY 4.0 License.

3. RESULTS

3.1 The overview of GLC_FCS30D land-cover dynamic maps

Figure 3 illustrates the schematic diagram of the GLC_FCS30D during 1985-2022, and two enlargements gave the land-cover changes in two typical areas, in which experienced obvious deforestation (Amazon rainforest area) and urban expansion (China’s Yangtze River Delta). Overall, the GLC_FCS30D accurately captured the global land-cover distributions (left figure), that is, the dominated land-cover types were forest, cropland, bare land and grassland, and the permanent snow and ice mainly distributed on the Greenland and high altitude mountains. In terms of capturing land-cover changes, the obvious deforestations in the Amazon rainforest were clearly captured in the GLC_FCS30D, especially during 2000-2010 (right figure). Similarly, the rapid urban expansion during 2000-2010 in the Yangtze River Delta was also revealed in our GLC_FCS30D dataset.

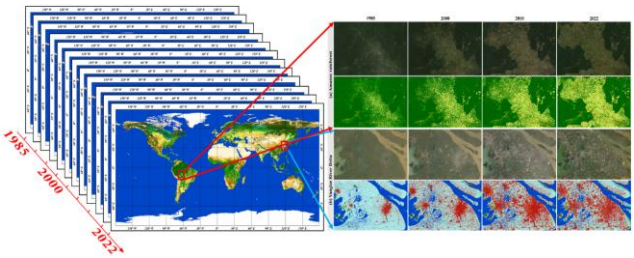

Figure 3. The schematic diagram of the GLC_FCS30D from 1985-2022.

3.2 Quantifying the accuracy of GLC_FCS30D products

Table 2 gives the quantitative accuracy metrics of GLC_FCS30D using the SRS_Val dataset in 2020. Overall, the GLC_FCS30D reached the overall accuracy of 80.88±0.27%. In terms of the specific land-cover type, the GLC_FCS30D achieved the higher accuracy in the cropland, forest, water body, permanent snow and ice and impervious surface and because 1) the former four types owned the obvious unique spectra characteristics or were the dominated land-cover types over the globe; 2) impervious surfaces were independently developed in the work of Zhang et al. (2022a). Comparatively, the grassland, shrubland and bare land had lower accuracies because they usually distributed on the semi-arid or arid areas, and there were confusions between them due to their similar spectra or the co-existence relationships (Zhang et al., 2024b).

Using the SRS_Val validation datset, we further calculated the accuracy metrics of six widely used global land-cover products (GlobeLand30 (Chen et al., 2015), FROM_GLC30 (Gong et al., 2013), GLC_FCS30 (Zhang et al., 2021b), FROM_GLC10 (Gong et al., 2019), ESA World Cover (Zanaga et al., 2021) and ESRI Land Cover (Karra et al., 2021)) in Figure 4. Overall, the GLC_FCS30 reached the highest overall accuracy, followed by the ESA World Cover, GlobeLand30, FROM_GLC10, FROM_GLC30 and ESRI Land Cover (Zhao et al., 2023). In terms of the producer’s and user’s accuracy, six products performed similar accuracies in most land-cover types, that is, performing better in forest, water body, snow and ice, while suffering poor performance in wetland, shrubland and grassland. It should be note that the ESRI Land Cover product performed the worst in six products because it overestimated the grassland and bare land into the shrubland, so the producer’s accuracuy of grassland and bare land in ESRI LC was obviously lower than other products. It should be noted that the Dynamic World (Brown et al., 2022) was excluded in the comparison because it was a near real-time dataset, that is, its performance was affected by the compositing method (synthesizing real-time dataset into the intra-annual products).

Table 2. The confusion matrix of GLC_FCS30D products against the SRS_Val validation dataset in 2020. The unit of the values in the table is percentage.

	CRP	FST	GRS	SHR	WET	WTR	TUD	IMP	BAL	PSI	Total	P.A.(SE)
CRP	15.44	0.79	0.68	0.39	0.09	0.03	0.00	0.17	0.12	0.00	17.70	87.2(0.54)
FST	0.51	28.71	0.32	0.81	0.37	0.02	0.01	0.06	0.11	0.00	30.93	92.8(0.31)
GRS	1.04	1.17	5.91	1.18	0.23	0.01	0.08	0.05	1.18	0.01	10.86	54.4(1.02)
SHR	0.56	1.80	0.86	5.39	0.16	0.01	0.02	0.05	0.50	0.00	9.36	57.6(1.09)
WET	0.07	0.47	0.16	0.16	4.05	0.35	0.03	0.02	0.22	0.00	5.52	73.4(1.27)
WTR	0.04	0.09	0.02	0.02	0.30	3.31	0.01	0.01	0.04	0.00	3.83	86.3(1.12)
TUD	0.01	0.12	0.17	0.17	0.02	0.03	2.44	0.00	0.47	0.02	3.45	70.8(1.65)
IMP	0.08	0.06	0.02	0.04	0.00	0.01	0.00	5.04	0.02	0.00	5.28	95.5(0.61)
BAL	0.13	0.05	0.78	0.59	0.04	0.05	0.58	0.05	9.24	0.13	11.63	79.5(0.80)
PSI	0.00	0.00	0.03	0.01	0.00	0.02	0.00	0.00	0.03	1.35	1.44	93.6(1.38)
Total	17.88	33.25	8.94	8.74	5.26	3.83	3.18	5.46	11.94	1.52		
U.A.	86.38	86.35	66.05	61.68	76.96	86.33	76.97	92.29	77.38	88.89		
(SE)	-0.55	-0.40	-1.07	-1.11	-1.20	-1.35	-1.60	-0.77	-0.82	-1.72		
O.A.	80.88% (±0.27%)											

Note: CRP: cropland, FST: forest, GRS: grassland, SHR: shrubland, WET: wetland, WTR: water body, TUD: tundra, IMP: impervious surface, BAL: bare land, PSI: permanent ice and snow, P.A.: producer’s accuracy, U.A.: user’s accuracy, SE: standard error.

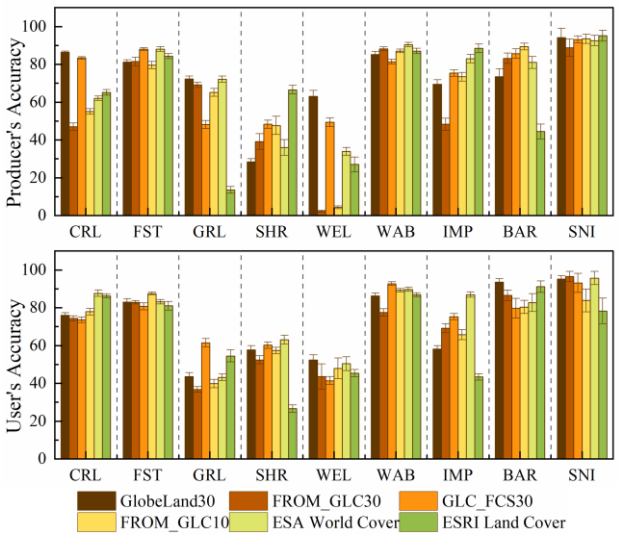

Figure 4. The accuracy metrics of six global 10 m/30 m land-cover products using the SRS_Val dataset.

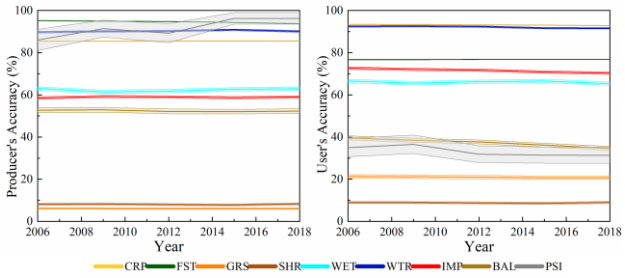

Figure 5. The time-series accuracy variations (producer’s accuracy and user’s accuracy) of GLC_FCS30D based on the LUCAS validation datasets.

Figure 5 illustrates the time-series accuracy variations using the LUCAS validation datasets, which was open-access and the largest validation dataset (containing 1090863 points) over the European Union during the period of 2006-2018 (d'Andrimont et al., 2020; Gao et al., 2020). Overall, the GLC_FCS30D achieved the stable performance on the temporal variations, and performed better over the forest, cropland and water-body (dominated land-cover types in the European Union), and suffered the lower P.A. or U.A. in some sparse land-cover types including: shrubland, grassland and bare land because of their complicated spectral characteristics and small size of validation point in the LUCAS. Similarly, our previous studies in Gao et al. (2020) also emphasized that the GLC_FCS30, FROM_GLC and GlobeLand30 (three widely used global land-cover products) achieved the higher accuracy in the dominated land-cover types, while suffered the commission or omission errors in the sparse land-cover types.

3.3 Analysis of global land-cover changes from the GLC_FCS30D products

Figure 6 presents the net area change of 10 major land-cover types in the GLC_FCS30D during 1985-2022. Intuitively, the most obvious characteristics of global land-cover change was the loss of forest and gain of cropland. The total loss of forest area reached 2.5 million km^2, while the gain of cropland area was 1.3 million km^2, which was consistent with the actual land-cover condition. Namely, a large amount of tropical rainforests were deforested to the cropland for fulfilling the growing demand for food (Potapov et al., 2021). Meanwhile, part of deforested forest was converted into the shrubland with increasement of 0.4 million km^2.

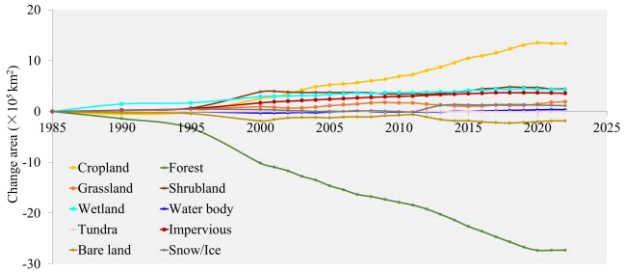

Figure 6. The gain and loss of 10 major land-cover types in GLC_FCS30D during 1985-2022, details were also given in Zhang et al. (2024b).

4. CONCLUSION AND PERSPECTIVE

Quantifying global land-cover changes at 30 m is important and necessary to analyse how human activities affect the global land surfaces. In this study, we proposed to stratify land surfaces into three thematic types (impervious surface, wetland and tidal flat) and other land-cover types, and then used the automated multitemporal classification methods to generate the time-series GISD30, GWL_FCS30D and GTF30D thematic products. Meanwhile, we combined the continuous change detection algorithm and local adaptive updating method to capture and update these land-cover changed areas. Next, after integrating the thematic products and the continuous change monitoring products, the novel GLC_FCS30D land-cover dynamic dataset was generated, which contained 35 fine land-cover types and spanned the period of 1985-2022. The accuracy assessment indicated that the GLC_FCS30D reached the overall accuracy of 80.88%, which meant that the developed GLC_FCS30D products can provide important data support in global climate change, biodiversity protection, and sustainable development goals. It should be noted that the GLC_FCS30D is also open access via: https://doi.org/10.5281/zenodo.8239305.

Combining stratified land-cover monitoring strategy and continuous change detection algorithm, we generate the first global 30 m fine land-cover dynamic products (GLC_FCS30D). It should be noted that a series of measures have been taken to guarantee the high quality of GLC_FCS30D, including continuous change detection, local adaptive modelling and spatiotemporal optimization. However, there were still several uncertainties: 1) the confidence of continuous change detection algorithm was affected the number of clear-sky Landsat imagery, that is, the land-cover changed accuracy before 2000 was lower than that after 2000. 2) The errors in the continuous change detection models might transform into the latter land-cover updating. We used the spatiotemporal optimization algorithm to minimize these transformed errors, but the residual effects still should be taken seriously. 3) The uncertainties in thematic land-cover change products (impervious surfaces, wetlands and tidal flats) also affected the accuracy of GLC_FCS30D because we overlap them into the GLC_FCS30D.

To further improve quality of the GLC_FCS30D, our further works would concentrate on: 1) integrating multisourced remote sensing data to achieve the annul land-cover change before 2000; 2) breaking through the land-cover change detection method for capturing the gradient-change processes (such as: forest degradation (Chen et al., 2023; Matricardi et al., 2020), afforestation or recovery); 3) clarifying the driver factors of land-cover changes for suppressing some natural-driven multiply changes, for example, the mutual transformation of grass, bare land and sparse vegetation in the semiarid/arid areas because of the differences in annual precipitation; 4) generating a time-series global validation dataset for comprehensively quantifying the accuracy metrics of GLC_FCS30D in capturing the land-cover changes.

ACKNOWLEDGEMENTS

The research works have been financial supported by the National Key Research and Development Program of China (Grant No. 2023YFB3907403) and the National Natural Science Foundation of China (42425001).

REFERENCES

Ban, Y., Gong, P., Giri, C., 2015. Global land cover mapping using Earth observation satellite data: Recent progresses and challenges. ISPRS Journal of Photogrammetry and Remote Sensing 103, 1-6.

Brown, C.F., Brumby, S.P., Guzder-Williams, B., Birch, T., Hyde, S.B., Mazzariello, J., Czerwinski, W., Pasquarella, V.J., Haertel, R., Ilyushchenko, S., Schwehr, K., Weisse, M., Stolle, F., Hanson, C., Guinan, O., Moore, R., Tait, A.M., 2022. Dynamic World, Near real-time global 10 m land use land cover mapping. Scientific Data 9.

Chen, J., Chen, J., Liao, A., Cao, X., Chen, L., Chen, X., He, C., Han, G., Peng, S., Lu, M., Zhang, W., Tong, X., Mills, J., 2015. Global land cover mapping at 30m resolution: A POK-based operational approach. ISPRS Journal of Photogrammetry and Remote Sensing 103, 7-27.

Chen, S., Woodcock, C., Dong, L., Tarrio, K., Mohammadi, D., Olofsson, P., 2023. Review of drivers of forest degradation and deforestation in Southeast Asia. Remote Sensing Applications: Society and Environment, 101129.

d'Andrimont, R., Verhegghen, A., Meroni, M., Lemoine, G., Strobl, P., Eiselt, B., Yordanov, M., Martinez-Sanchez, L., van der Velde, M., 2020. LUCAS Copernicus 2018: Earth

Observation relevant in-situ data on land cover throughout the European Union.
Defourny, P., Kirches, G., Brockmann, C., Boettcher, M., Peters, M., Bontemps, S., Lamarche, C., Schlerf, M., M., S., 2016. Land Cover CCI: Product User Guide Version 2.
Dyer, K., Christie, M., Wright, E., 2000. The classification of intertidal mudflats. Continental Shelf Research 20, 1039-1060.
Florczyk, A., Corbane, C., Ehrlich, D., Freire, S., Kemper, T., Maffenini, L., Melchiorri, M., Pesaresi, M., Politis, P., Schiavina, M., 2019. GHSL Data Package 2019. Luxembourg. EUR 29788.
Friedl, M.A., Sulla-Menashe, D., Tan, B., Schneider, A., Ramankutty, N., Sibley, A., Huang, X., 2010. MODIS Collection 5 global land cover: Algorithm refinements and characterization of new datasets. Remote Sensing of Environment 114, 168-182.
Friedl, M.A., Woodcock, C.E., Olofsson, P., Zhu, Z., Loveland, T., Stanimirova, R., Arevalo, P., Bullock, E., Hu, K.-T., Zhang, Y., Turlej, K., Tarrio, K., McAvoy, K., Gorelick, N., Wang, J.A., Barber, C.P., Souza, C., 2022. Medium Spatial Resolution Mapping of Global Land Cover and Land Cover Change Across Multiple Decades From Landsat. Frontiers in Remote Sensing 3.
Gao, Y., Liu, L., Zhang, X., Chen, X., Mi, J., Xie, S., 2020. Consistency Analysis and Accuracy Assessment of Three Global 30-m Land-Cover Products over the European Union using the LUCAS Dataset. Remote Sensing 12, 3479.
Gong, P., Li, X., Wang, J., Bai, Y., Chen, B., Hu, T., Liu, X., Xu, B., Yang, J., Zhang, W., Zhou, Y., 2020. Annual maps of global artificial impervious area (GAIA) between 1985 and 2018. Remote Sensing of Environment 236, 111510.
Gong, P., Liu, H., Zhang, M., Li, C., Wang, J., Huang, H., Clinton, N., Ji, L., Li, W., Bai, Y., Chen, B., Xu, B., Zhu, Z., Yuan, C., Ping Suen, H., Guo, J., Xu, N., Li, W., Zhao, Y., Yang, J., Yu, C., Wang, X., Fu, H., Yu, L., Dronova, I., Hui, F., Cheng, X., Shi, X., Xiao, F., Liu, Q., Song, L., 2019. Stable classification with limited sample: transferring a 30-m resolution sample set collected in 2015 to mapping 10-m resolution global land cover in 2017. Science Bulletin 64, 370-373.
Gong, P., Wang, J., Yu, L., Zhao, Y., Zhao, Y., Liang, L., Niu, Z., Huang, X., Fu, H., Liu, S., Li, C., Li, X., Fu, W., Liu, C., Xu, Y., Wang, X., Cheng, Q., Hu, L., Yao, W., Zhang, H., Zhu, P., Zhao, Z., Zhang, H., Zheng, Y., Ji, L., Zhang, Y., Chen, H., Yan, A., Guo, J., Yu, L., Wang, L., Liu, X., Shi, T., Zhu, M., Chen, Y., Yang, G., Tang, P., Xu, B., Giri, C., Clinton, N., Zhu, Z., Chen, J., Chen, J., 2013. Finer resolution observation and monitoring of global land cover: first mapping results with Landsat TM and ETM+ data. International Journal of Remote Sensing 34, 2607-2654.
Grekousis, G., Mountrakis, G., Kavouras, M., 2015. An overview of 21 global and 43 regional land-cover mapping products. International Journal of Remote Sensing 36, 5309-5335.
Guo, M., Li, J., Sheng, C., Xu, J., Wu, L., 2017. A Review of Wetland Remote Sensing. Sensors 17.
Hu, S., Niu, Z., Chen, Y., 2017. Global Wetland Datasets: a Review. Wetlands 37, 807-817.
Jia, M., Wang, Z., Mao, D., Ren, C., Wang, C., Wang, Y., 2021. Rapid, robust, and automated mapping of tidal flats in China using time series Sentinel-2 images and Google Earth Engine. Remote Sensing of Environment 255, 112285.
Karra, K., Kontgis, C., Statman-Weil, Z., Mazzariello, J.C., Mathis, M., Brumby, S.P., 2021. Global land use / land cover with Sentinel 2 and deep learning. 4704-4707.
Liu, L., Zhang, X., Gao, Y., Chen, X., Shuai, X., Mi, J., 2021. Finer-Resolution Mapping of Global Land Cover: Recent Developments, Consistency Analysis, and Prospects. Journal of Remote Sensing 2021, 1-38.
Matricardi, E.A.T., Skole, D.L., Costa, O.B., Pedlowski, M.A., Samek, J.H., Miguel, E.P., 2020. Long-term forest degradation surpasses deforestation in the Brazilian Amazon. Science 369, 1378-1382.
Murray, N.J., Phinn, S.R., DeWitt, M., Ferrari, R., Johnston, R., Lyons, M.B., Clinton, N., Thau, D., Fuller, R.A., 2019. The global distribution and trajectory of tidal flats. Nature 565, 222-225.
Murray, N.J., Worthington, T.A., Bunting, P., Duce, S., Hagger, V., Lovelock, C.E., Lucas, R., Saunders, M.I., Sheaves, M., Spalding, M., 2022. High-resolution mapping of losses and gains of Earth’s tidal wetlands. Science 376, 744-749.
Olofsson, P., Foody, G.M., Herold, M., Stehman, S.V., Woodcock, C.E., Wulder, M.A., 2014. Good practices for estimating area and assessing accuracy of land change. Remote Sensing of Environment 148, 42-57.
Otsu, N., 1979. A threshold selection method from gray-level histograms. IEEE transactions on systems, man, and cybernetics 9, 62-66.
Pekel, J.F., Cottam, A., Gorelick, N., Belward, A.S., 2016. High-resolution mapping of global surface water and its long-term changes. Nature 540, 418-422.
Potapov, P., Hansen, M.C., Pickens, A., Hernandez-Serna, A., Tyukavina, A., Turubanova, S., Zalles, V., Li, X., Khan, A., Stolle, F., Harris, N., Song, X.-P., Baggett, A., Kommareddy, I., Kommareddy, A., 2022. The Global 2000-2020 Land Cover and Land Use Change Dataset Derived From the Landsat Archive: First Results. Frontiers in Remote Sensing 3.
Potapov, P., Turubanova, S., Hansen, M.C., Tyukavina, A., Zalles, V., Khan, A., Song, X.-P., Pickens, A., Shen, Q., Cortez, J., 2021. Global maps of cropland extent and change show accelerated cropland expansion in the twenty-first century. Nature Food 3, 19-28.
Radoux, J., Lamarche, C., Van Bogaert, E., Bontemps, S., Brockmann, C., Defourny, P., 2014. Automated Training Sample Extraction for Global Land Cover Mapping. Remote Sensing 6, 3965-3987.
Roy, D.P., Wulder, M.A., Loveland, T.R., C.E, W., Allen, R.G., Anderson, M.C., Helder, D., Irons, J.R., Johnson, D.M., Kennedy, R., Scambos, T.A., Schaaf, C.B., Schott, J.R., Sheng, Y., Vermote, E.F., Belward, A.S., Bindschadler, R., Cohen, W.B., Gao, F., Hipple, J.D., Hostert, P., Huntington, J., Justice, C.O., Kilic, A., Kovalskyy, V., Lee, Z.P., Lymburner, L., Masek, J.G., McCorkel, J., Shuai, Y., Trezza, R., Vogelmann, J., Wynne, R.H., Zhu, Z., 2014. Landsat-8: Science and product vision for terrestrial global change research. Remote Sensing of Environment 145, 154-172.
Song, X.P., Hansen, M.C., Stehman, S.V., Potapov, P.V., Tyukavina, A., Vermote, E.F., Townshend, J.R., 2018. Global land change from 1982 to 2016. Nature 560, 639-643.
Stehman, S.V., Olofsson, P., Woodcock, C.E., Herold, M., Friedl, M.A., 2012. A global land-cover validation data set, II: augmenting a stratified sampling design to estimate accuracy by region and land-cover class. International Journal of Remote Sensing 33, 6975-6993.
Wang, N., Zhang, X., Yao, S., Wu, J., Xia, H., 2022. How Good Are Global Layers for Mapping Rural Settlements? Evidence from China. Land 11, 1308.
Wang, Y., Sun, Y., Cao, X., Wang, Y., Zhang, W., Cheng, X., 2023. A review of regional and Global scale Land Use/Land Cover (LULC) mapping products generated from satellite remote sensing. ISPRS Journal of Photogrammetry and Remote Sensing 206, 311-334.
Winkler, K., Fuchs, R., Rounsevell, M., Herold, M., 2021. Global land use changes are four times greater than previously estimated. Nat Commun 12, 2501.
Woodcock, C.E., Allen, R.G., Anderson, M.C., 2008. Free access to Landsat imagery. Science 320, 1011.

Xian, G.Z., Smith, K., Wellington, D., Horton, J., Zhou, Q., Li, C., Auch, R., Brown, J.F., Zhu, Z., Reker, R.R., 2022. Implementation of the CCDC algorithm to produce the LCMAP Collection 1.0 annual land surface change product. Earth Syst. Sci. Data 14, 143-162.

Yang, J., Huang, X., 2021. The 30 m annual land cover dataset and its dynamics in China from 1990 to 2019. Earth Syst. Sci. Data 13, 3907-3925.

Zanaga, D., Van De Kerchove, R., De Keersmaecker, W., Souverijns, N., Brockmann, C., Quast, R., Wevers, J., Grosu, A., Paccini, A., Vergnaud, S., 2021. ESA WorldCover 10 m 2020 v100. Zenodo: Geneve, Switzerland.

Zhang, H.K., Roy, D.P., 2017. Using the 500 m MODIS land cover product to derive a consistent continental scale 30 m Landsat land cover classification. Remote Sensing of Environment 197, 15-34.

Zhang, X., Liu, L., Chen, X., Gao, Y., Jiang, M., 2021a. Automatically Monitoring Impervious Surfaces Using Spectral Generalization and Time Series Landsat Imagery from 1985 to 2020 in the Yangtze River Delta. Journal of Remote Sensing 2021, 1-16.

Zhang, X., Liu, L., Chen, X., Gao, Y., Xie, S., Mi, J., 2021b. GLC_FCS30: global land-cover product with fine classification system at 30 m using time-series Landsat imagery. Earth Syst. Sci. Data 13, 2753-2776.

Zhang, X., Liu, L., Chen, X., Xie, S., Gao, Y., 2019. Fine Land-Cover Mapping in China Using Landsat Datacube and an Operational SPECLib-Based Approach. Remote Sensing 11, 1056.

Zhang, X., Liu, L., Wang, J., Zhao, T., Liu, W., Chen, X., 2023a. Automated mapping of global 30 m tidal flats using time-series Landsat imagery: algorithm and products. Journal of Remote Sensing 3.

Zhang, X., Liu, L., Wang, Y., Hu, Y., Zhang, B., 2018. A SPECLib-based operational classification approach: A preliminary test on China land cover mapping at 30 m. International Journal of Applied Earth Observation and Geoinformation 71, 83-94.

Zhang, X., Liu, L., Wu, C., Chen, X., Gao, Y., Xie, S., Zhang, B., 2020. Development of a global 30 m impervious surface map using multisource and multitemporal remote sensing datasets with the Google Earth Engine platform. Earth Syst. Sci. Data 12, 1625-1648.

Zhang, X., Liu, L., Zhao, T., Chen, X., Lin, S., Wang, J., Mi, J., Liu, W., 2023b. GWL_FCS30: a global 30 m wetland map with a fine classification system using multi-sourced and time-series remote sensing imagery in 2020. Earth Syst. Sci. Data 15, 265-293.

Zhang, X., Liu, L., Zhao, T., Gao, Y., Chen, X., Mi, J., 2022a. GISD30: global 30 m impervious-surface dynamic dataset from 1985 to 2020 using time-series Landsat imagery on the Google Earth Engine platform. Earth Syst. Sci. Data 14, 1831-1856.

Zhang, X., Liu, L., Zhao, T., Wang, J., Liu, W., Chen, X., 2024a. Mapping global annual wetlands at 30 m with a fine classification system from 2000 to 2022. Sci Data, Under Review.

Zhang, X., Zhao, T., Xu, H., Liu, W., Wang, J., Chen, X., Liu, L., 2024b. GLC_FCS30D: The first global 30-m land-cover dynamic monitoring product with a fine classification system from 1985 to 2022 using dense time-series Landsat imagery and continuous change-detection method. Earth Syst. Sci. Data 16, 1-32.

Zhang, Z., Xu, N., Li, Y., Li, Y., 2022b. Sub-continental-scale mapping of tidal wetland composition for East Asia: A novel algorithm integrating satellite tide-level and phenological features. Remote Sensing of Environment 269, 112799.

Zhao, T., Zhang, X., Gao, Y., Mi, J., Liu, W., Wang, J., Jiang, M., Liu, L., 2023. Assessing the Accuracy and Consistency of Six Fine-Resolution Global Land Cover Products Using a Novel Stratified Random Sampling Validation Dataset. Remote Sensing 15, 2285.

Zhu, Z., Woodcock, C.E., 2014. Continuous change detection and classification of land cover using all available Landsat data. Remote Sensing of Environment 144, 152-171.

Zhu, Z., Woodcock, C.E., Olofsson, P., 2012. Continuous monitoring of forest disturbance using all available Landsat imagery. Remote Sensing of Environment 122, 75-91.